Plasmonics (2022) 17:181–191
https://doi.org/10.1007/s11468-021-01513-7

High-performance Opening-up Dual-core Photonic Crystal Fiber Sensors Based on Surface Plasmon Resonance

Soghra Ghahramani[1] · Jamal Barvestani[1] · Bahar Meshginqalam[1]

Received: 4 May 2021 / Accepted: 26 July 2021 / Published online: 2 August 2021

Abstract

Nowadays, plasmonic sensors based on photonic crystal fiber (PCF) attracted a great deal of attention in the field of optical sensing. Opening-up dual-core photonic crystal fibers based on surface plasmon resonance (SPR) are numerically demonstrated and analyzed for detecting a wide refractive index (RI) range by the finite-difference time-domain method (FDTD). Wavelength and amplitude integration methods as well as figures of merit are used to investigate the sensing performance. For improving sensing performance, a large hole between two cores in the opening-up section is introduced. The opening-up section as a sensing channel is coated with a gold film and a thin titanium dioxide (TiO_2) layer. By surface engineering including imposing of grating on the gold film, specification of optimized values of different layers located near the surface and sensing performance are investigated. Next, the effect of the fiber structural parameters is analyzed to enhance SPR and fundamental core mode coupling. The proposed sensor revealed maximum wavelength and amplitude sensitivities of 15,167 $\left(\frac{nm}{RIU}\right)$ and 207.19 $\left(RIU^{-1}\right)$, respectively. Due to the ease of infiltration of analyte and gold coating and thanks to the high wavelength and amplitude sensitivity, the sensors can be a promising candidate for physical and chemical sensing.

Keywords Photonic crystal fiber · Dual-core sensor · Surface plasmon resonance · Sensitivity · FDTD

Introduction

Surface plasmon resonance (SPR) refers to an electromagnetic phenomenon, which is generated by the combination of free electron oscillations and a transverse magnetic polarized electromagnetic wave on the surface between dielectric medium and metal film [1, 2]. Due to outstanding features such as label-free monitoring, high sensitivity, and real-time detection, as well as owning multifarious applications such as environmental monitoring, medical diagnostics and food safety, polarization filters, and absorbers, SPR has achieved unprecedented progress in the realm of sensors [2–4]. Kretschman proposed a configuration of SPR sensors based on prism coupling [2, 3, 5]. Bulky apparatus, heavy weight, inability of remote detection, and inflexibility were major inefficiencies of this configuration, which are refined by the advent of photonic crystal fiber SPR sensors by Jorgenson where gold was used to create the SPR phenomenon [2–5]. Owning outstanding characteristics such as tunable effective refractive index in the fiber core, controllable birefringence, and superior light confining capabilities, PCF-SPR sensors have drawn a great deal of attention [2, 4]. SPR-based sensors, according to PCF's properties, use several sensing configurations mainly including internal and external metal coating-based sensing approaches. In internal sensing, the analyte is infiltrated in the selective micro-meter-sized air holes [6, 7]. Rifat et al. proposed a SPR-PCF sensor in which a large air-hole beside the core for efficient light coupling between the cores and SPR modes is introduced [8]. In addition, this large air hole will facilitate material coating and effective analyte flow. Conversely, the external metal coating–based sensing method is commonly used; not only does it provide more flexibility, but also it is easier compared to covering the inner air holes as well [8, 9]. To date, various externally coated SPR-based PCF sensors, which can include D-shaped structures, have been reported. A dual-polarized spiral photonic crystal fiber based on surface plasmon resonance was proposed in ref. [9]. They showed wavelength sensitivity of 4600 $\frac{nm}{RIU}$ and amplitude sensitivity of 420.4 RIU^{-1} in the y-polarized mode. In the x-polarized mode,

✉ Jamal Barvestani
barvestani@tabrizu.ac.ir

[1] Faculty of Physics, University of Tabriz, Tabriz, Iran

the maximum wavelength sensitivity is 4300 $\frac{nm}{RIU}$ and the amplitude sensitivity is 371.5 RIU^{-1}. A dual-core PCF sensor using gold as a plasmonic material with high value of amplitude sensitivity but lower value of wavelength sensitivity was reported by Paul et al. [10]. In 2020, Han et al. designed a large detection-range plasmonic sensor based on an H-shaped PCF with maximum wavelength sensitivity of 25,900 $\frac{nm}{RIU}$ [11]. Recently, SPR-based PCF sensors have encountered two main problems. First, due to micro-sized air holes, metal coating and analyte filling are challenging procedures [8, 9, 11, 12]. The second problem is about low RI or high RI PCF-SPR sensors are due to their narrow RI range of detection [6, 11]. This problem can be solved by using the total internal refraction and the crystal geometrical engineering.

Opening-up micro-structured optical fibers (MOF), such as D-shaped or exposed-core MOF-SPR sensors [13–15], are the promising approaches to facilitate the infiltration problem. An opening-up dual-core microstructure optical fiber–based plasmonic sensor with a large detection range and linear sensitivity was proposed in [14] and showed the maximal sensitivity of 4900 $\frac{nm}{RIU}$ when the RI of the analyte is close to that of the fiber background material. To overcome the problems aforementioned, in this paper we propose an opening-up plasmonic sensor based on dual-core PCF which can be operated in the range from 1.42 to 1.46. For improving sensing performance, a large hole between two cores in the opening-up slot is introduced. The opening-up section as a sensing channel is coated with gold film where a thin titanium dioxide (TiO_2) layer is placed between gold and analyte in only this hole part. Next, with imposing changes in the surface of this part including applying grated gold film and sandwiching a thin layer of TiO_2 between fiber surface and gold, we investigate the effect of these structure variations on sensing performance. Recently, an investigation revealed that the gold layer coated on the fiber can be flaked off from the fiber [6]. TiO_2 accompanied by a gold layer can conquer the adhesion problem of gold to fiber [16]. Regarding sensitivity, this sensor shows a high sensitivity value better than that in [14]. The opening-up part is directly filled with analyte and supports possibility for real-time sensing.

Design and Numerical Method

Figure 1(a) shows the schematic representation of our proposed sensor, comprising an open slot which is coated by a gold layer. This part acts as a sensing channel and can be directly in contact with the analyte. In addition, to improve the sensing performance, we introduce a large hole with diameter of $2r_c$ between two cores in the sensing channel. This is because evanescent waves can enhance the resonance effect, which may improve the sensitivity significantly. This dual-core SPR-PCF sensor has been designed by arranging the air holes in a hexagonal lattice with pitch size Λ. For introducing two solid cores, two air holes in

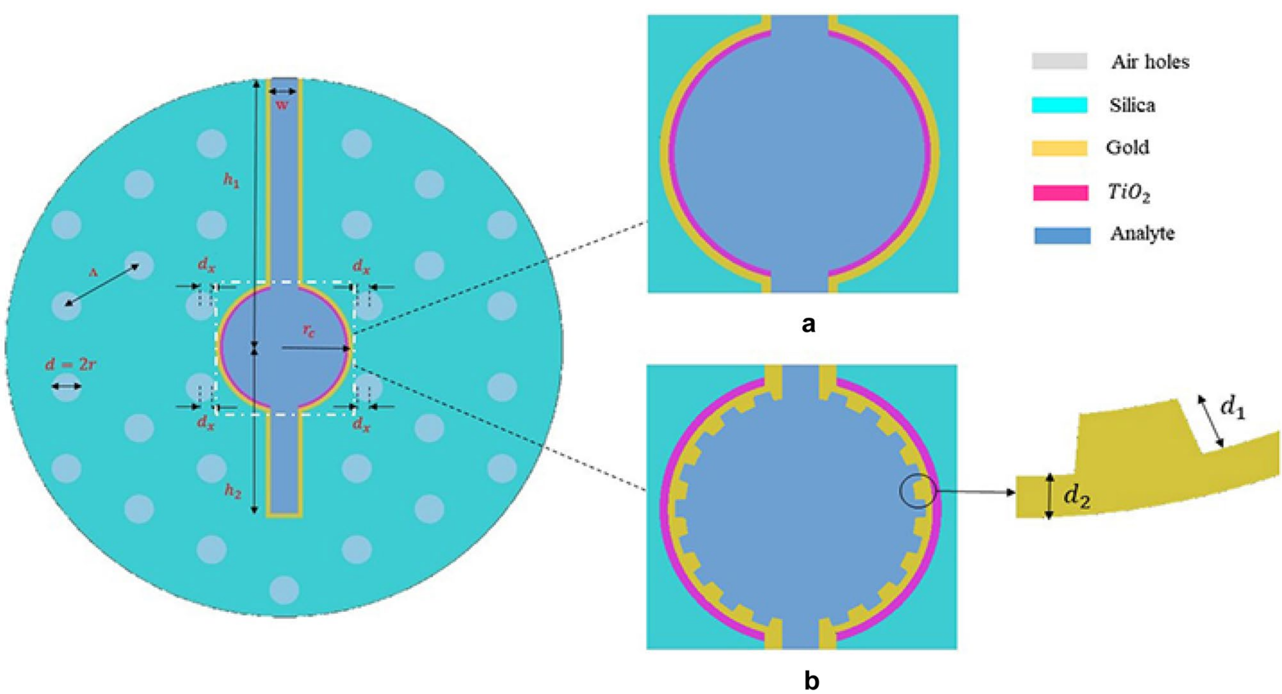

Fig. 1 Cross-section view of the DC-PCF-SPR sensor magnifying of central large hole **a** with Au and TiO_2 thin layers between Au and analyte **b** with Au nano-continued grating layer and thin TiO_2 layer between fiber material and Au

the second ring of the hexagonal lattice are removed. The air holes with radius r work as a low refractive index cladding, enabling mode guidance in the fiber core. Furthermore, we applied a shift by a distance dx in the center of four selected air holes which is situated near the large hole from their original position. Shifting holes lead to achievement of an optimum structure which is needed to get high sensitivity. With the purpose of increasing the plasmon excitation, a thin layer of TiO_2 with the thickness of t_{TiO_2} is deposited on gold.

Our sensor is modeled using the following parameters: $\Lambda = 2.26\ \mu m$, $r = 0.4\ \mu m$, $dx = 0.3\ \mu m$, $r_c = 1.85\ \mu m$, $t_{Au} = 40\ nm$, $t_{TiO_2} = 7\ nm$, $w = 1\ \mu m$, $h_1 = 7.5\ \mu m$, $h_2 = 4.75\ \mu m$. From the fabrication point of view, considering the similar design, the open-slot part can be made by femtosecond laser micromachining [17], focused ion-beam milling [18], or chemical etching of the original side-hole PCF [19] or can be directly drawn by creating an opening at the preform stage of the fiber fabrication [20]. The gold grating was introduced to modulate the resonance wavelength and enhance the RI sensitivity. Again considering similar designs, there are some methods for the creation of metallic grating such as electron beam etching technology [21], high-pressure microfluidic chemical deposition [22], two-photon direct laser writing technique [23], and electron beam etching technology [24]. The refractive indices of background material and air-holes are supposed to be 1.45 and 1, respectively, and gold permittivity is modeled from Johnson and Christy data [25]. The RI of TiO_2 is calculated by the following [26]:

$$n^2_{TiO_2} = 5.913 + \frac{0.2441}{\lambda^2 - 0.0803}, \qquad (1)$$

where λ is in micrometers.

A perfectly matched layer (PML) is applied as a scattering boundary condition. The FDTD method is employed to investigate the sensor performance. Figure 1(b) shows the same structure associated with some changes in the surface of the proposed sensor. Indeed, grated Au is used as a plasmonic material in the large-hole part and the TiO_2 thin layer is deposited between fiber and gold due to adhesion assistance. The optimized parameters are as follows: segmented Au film thickness $d_1 = 25\ nm$ and continuous Au film thickness $d_2 = 15\ nm$, total segment number $N = 28$, $t_{TiO_2} = 5\ nm$. Other geometric parameters are the same as mentioned before.

The key factor to analyzing the performance of PCF-SPR sensors is calculation of the confinement loss of the fundamental core mode. The imaginary part of the effective refractive index (n_{eff}) is used to determine the confinement loss and can be expressed as the following [27]:

$$\alpha_c\left(\frac{dB}{cm}\right) = 8.686 \times \frac{2\pi}{\lambda(\mu m)} Im\left(n_{eff}\right) \times 10^4, \qquad (2)$$

where λ is the operating wavelength. The proposed sensor has two guiding modes (a) x-polarization and (b) y-polarization. In the dual-core PCF-SPR sensors, for x-polarization and y-polarization, the odd and even modes are excited simultaneously. But here the confinement loss of the odd mode for y-polarization is the largest, which means that the SPR mode couples with the odd mode for y-polarization more strongly than the other polarization. Hence, we focus on the odd core mode for y-polarization in the following numerical analysis.

Results and Discussion

Different structural parameters such as radius of central large hole (r_c), width of slot (w), distance between center and end of slot (h_2), and position of the neighboring holes of the central hole (dx) are examined, and optimum parameters are selected throughout this work. Performance of the proposed sensor is numerically carried out by the FDTD method in the wavelength range of 0.975–1.7 μm, and fundamental core mode, SPR mode, and dispersion relation are investigated for the proposed sensor. The first part of the results is associated with the configuration of Fig. 1(a). The electric field profile of the odd fundamental core, SPR, and coupled core-SPR modes at the resonance wavelength are depicted in Fig. 2a–c, respectively. Obviously, in the resonance condition most of the energy is confined in solid core regions, and only a small part of energy penetrates to the metal film surface (see Fig. 2c). This penetration causes a peak in the loss spectrum which can be analyzed by the dispersion relationship between the fundamental core mode and the SPR mode as it is shown in Fig. 2d. In fact, coupling between the core and plasmonic modes occurs when the propagation constant and wave vector of two modes become equal. This condition is known as phase matching.

As it is clear from this figure, the real part of n_{eff} of both modes coincides at the wavelength of 1.4589 μm, called resonance wavelength where corresponding loss is 89.97 $\frac{dB}{cm}$.

The real part of the effective index of the plasmonic mode is highly dependent on the small variation of analyte RI. When the RI of analyte is changed, it leads to the resonance wavelength shifts. Using the mentioned optimized parameters, the loss curves of the proposed dual-core SPR-PCF sensor for different RI of analyte ranging from 1.42 to 1.46 in the absence of TiO_2 layer are plotted and shown in Fig. 3.

As it is clearly shown in Fig. 3, with increasing n_a up to 1.45, a red shift of resonance wavelengths is found, and

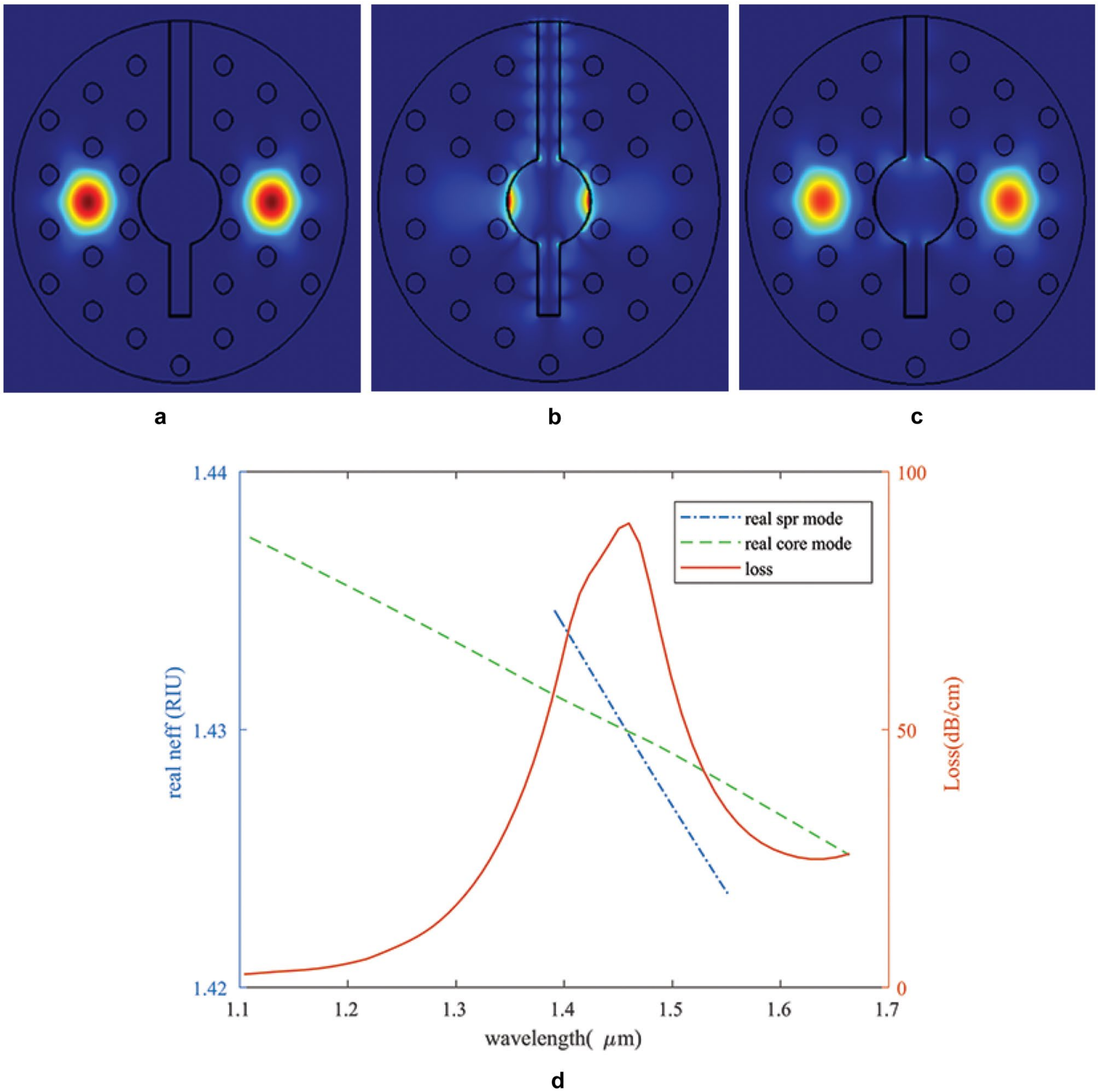

Fig. 2 Electric field distribution of the **a** *y*-polarized odd core mode, **b** odd SPP mode, **c** resonance condition, and **d** dispersion relation of core mode (green), SPR mode (blue), and loss spectrum (red) of core mode for $n_a = 1.43, t_{TiO_2} = 7\ nm, t_{Au} = 40\ nm$

the loss spectra noticeably increase. But, when n_a changes from 1.45 to 1.46, the resonance wavelength shifts towards a longer wavelength, while loss decreases. In fact, when the refractive index changes from 1.45 to 1.46, a significant decrease in the effective refractive index occurs as the wavelength increases, which cause a reduction in RI contrast between core and SPP modes. The coupling between these modes is weakened which leads to loss decrement. Next, we have examined the loss curves of the proposed sensor by introducing an extra overlayer of TiO_2. Interestingly, it can be observed that by applying the TiO_2 layer, a monotonic increasing trend in resonance wavelength and its intensity is achieved, as it is shown in Fig. 4.

With increasing RI of analyte n_a, the peak of loss shifts toward a longer wavelength and confinement loss increases as well.

It is convenient to investigate the sensor performance from the loss curve by using the wavelength and amplitude interrogation methods. The ratio of peak wavelength change to refractive index is known as the wavelength sensitivity, and it is computed as below [28]:

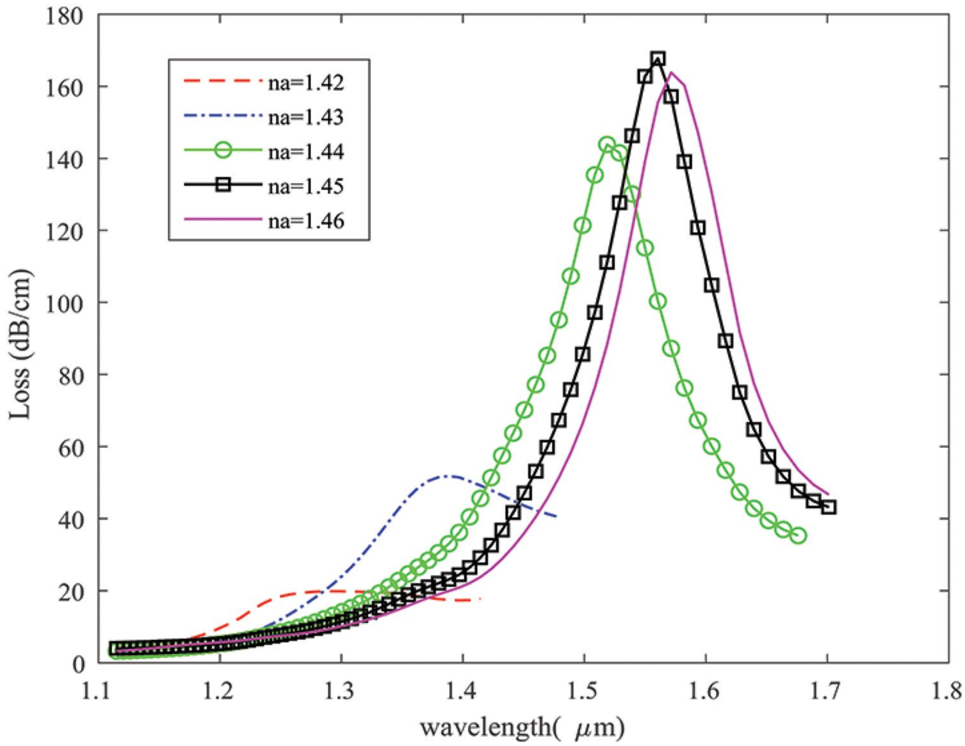

Fig. 3 Loss curves as a function of operating wavelength of the proposed sensor for different analytes without TiO_2 configuration $(t_{TiO_2} = 0\ nm), t_{Au} = 40\ nm$

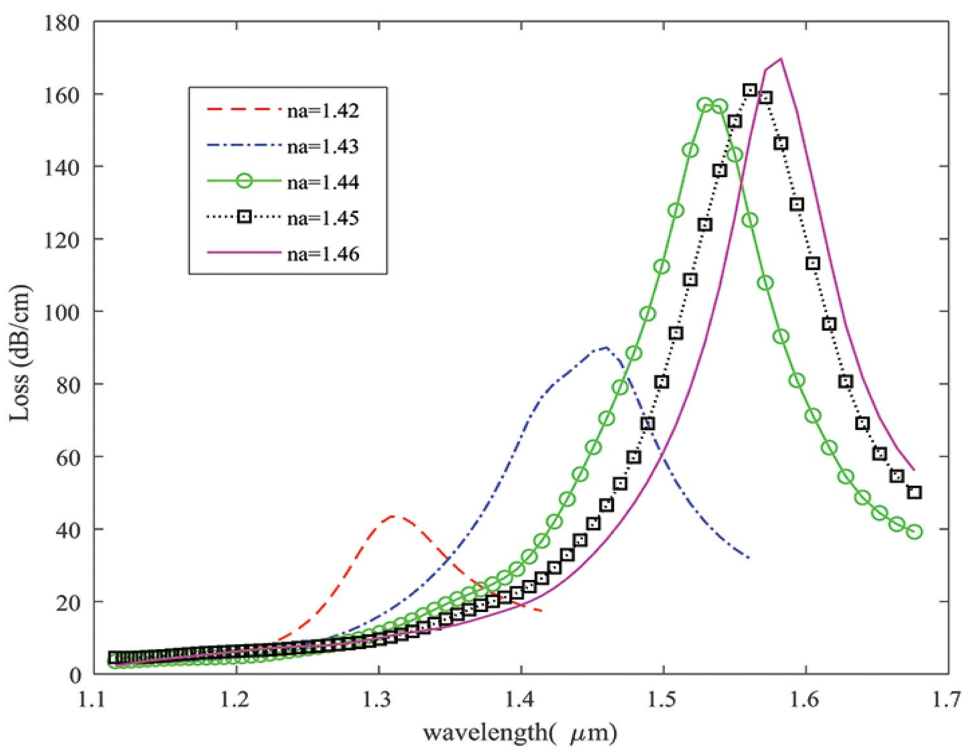

Fig. 4 Loss curves as a function of operating wavelength of the proposed sensor for different analytes for $t_{TiO_2} = 7\ nm, t_{Au} = 40\ nm$

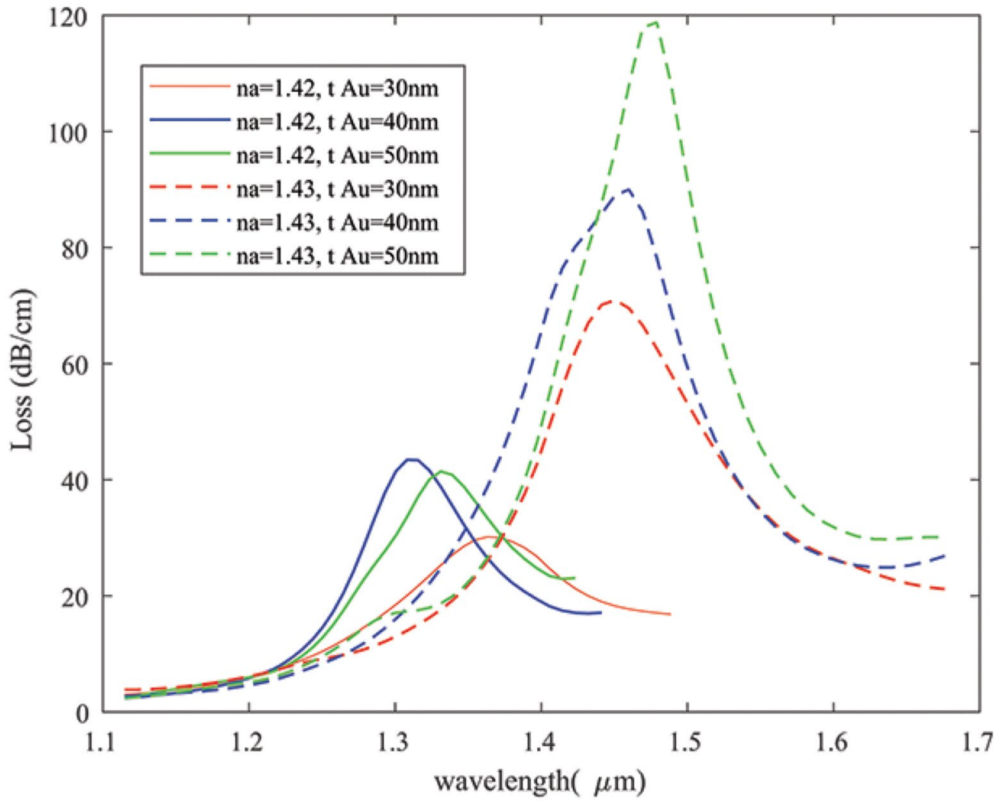
na=1.42, t Au=30nm
na=1.42, t Au=40nm
na=1.42, t Au=50nm
na=1.43, t Au=30nm
na=1.43, t Au=40nm
na=1.43, t Au=50nm
Loss (dB/cm)
wavelength(μm)
0
20
40
60
80
100
120
1.1
1.2
1.3
1.4
1.5
1.6
1.7

a

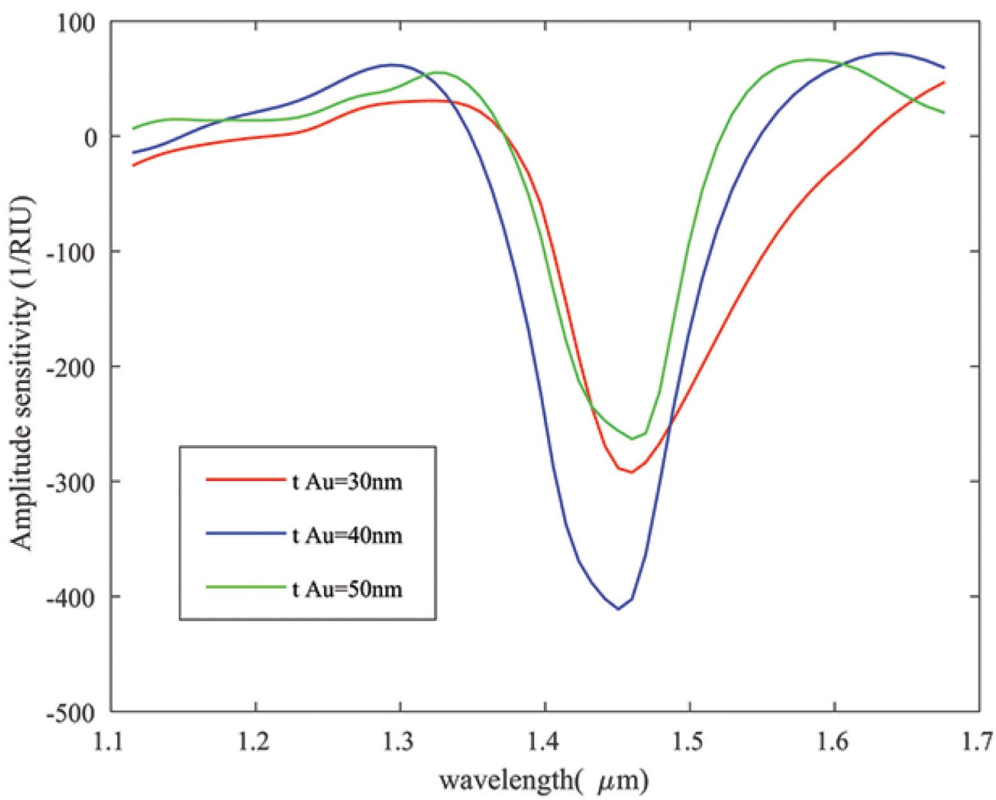
t Au=30nm
t Au=40nm
t Au=50nm
Amplitude sensitivity (1/RIU)
wavelength(μm)
100
0
-100
-200
-300
-400
-500
1.1
1.2
1.3
1.4
1.5
1.6
1.7

b

◂**Fig. 5** **a** Loss variation for different thicknesses of gold layer of the proposed sensor and **b** amplitude sensitivity for different thicknesses of gold layer with $t_{TiO_2} = 7\ nm$

$$s_\lambda = \frac{\partial \lambda_{peak}}{\partial n_a}\left[\frac{nm}{RIU}\right]. \tag{3}$$

Also, the amplitude sensitivity can be evaluated by the following equation [28]:

$$S_A = -\frac{1}{\alpha(\lambda, n_a)} \times \frac{\partial \alpha(\lambda, n_a)}{\partial n_a}\left[RIU^{-1}\right], \tag{4}$$

where $\alpha(\lambda, n_a)$ is the confinement loss at different RI. With these definitions, the proposed sensor shows wavelength sensitivities of 15,167, 6894, 3158, and 2179 $\frac{nm}{RIU}$, respectively, when the analyte's RI changes from 1.42 to 1.46 with a step of 0.01. The maximum wavelength sensitivity is 15,167 $\frac{nm}{RIU}$ which is higher than that previously proposed in [14] which is a similar work, and also it is higher than the maximum wavelength sensitivity of the proposed sensor in the absence of TiO_2 (13,024 $\frac{nm}{RIU}$). Furthermore, the amplitude sensitivities obtained are 207.19, 62.55, 35.40, and 22.91 RIU^{-1}, correspondingly.

Generally, geometric parameters have a dominant effect on the sensor performance. The effects of the change of Au and TiO_2 thickness on loss spectra are depicted in Figs. 5 and 6, respectively. As it is seen from Fig. 5a with increasing gold thickness from 30 to 50 nm, loss increases, and wavelength redshifts for the RI analyte of 1.43, while due to the different phase matching conditions (for two different analytes), the ascending trend is absent for the case of $n_a = 1.42$. Figure 5b shows the amplitude sensitivity; the maximum S_A of 411.1 RIU^{-1} is obtained for $t_{Au} = 40\ nm$ with n_a varying from 1.42 to 1.43. These results are summarized in Table 1 which included both wavelength and amplitude sensitivity for the proposed sensor with various thicknesses of gold. Considering wavelength and amplitude sensitivity, $t_{Au} = 40\ nm$ is chosen as optimum thickness of Au in our calculations.

By this value of t_{Au}, the effect of different TiO_2 thicknesses on loss curves is illustrated in Fig. 6 where wavelength sensitivity can be calculated by its data.

The obtained S_W for given TiO_2 thicknesses are 13,024, 12,538, 15,167, and 14,157 $\frac{nm}{RIU}$, respectively, in which $t_{TiO_2} = 7\ nm$ shows better sensitivity. Titanium dioxide has not only diminished the adhesion problem but because of its high refractive index, it strongly attracts the field from the core mode, and causes strong coupling between core and plasmonic mode [29].

Besides of sensitivity, another factor for analyzing sensor performance is figure of merit (FOM) which can be defined as the ratio of sensitivity to full width at half maximum (FWHM) as [30]:

$$FOM\left(RIU^{-1}\right) = \frac{sensitivity\left(\frac{nm}{RIU}\right)}{FWHM(nm)}. \tag{5}$$

Now then, the sensitivities and FOM of the proposed sensor are investigated for the wide range of analyte RI which are summarized in Table 2.

The proposed sensor shows the best performance in RI range of 1.42–1.43 with respect to wavelength and amplitude sensitivities and FOM. By increasing n_a, these sensing factors decrease monotonically.

The resolution of the sensor is also essential to determine the detection capability of the offered sensor and can be computed by [30]:

$$R(RIU) = \Delta n_a \times \Delta\lambda_{min}/\Delta\lambda_{peak}, \tag{6}$$

where $\Delta\lambda_{min}$ is assumed to be 0.1 nm. The maximum resolution of the proposed sensor is obtained as high as 6.6×10^{-6}. Therefore, the smallest change in analyte RI in order of 10^{-6} can be detected with a high degree of accuracy.

The last part of this work is devoted to the effect of grating on the surface of structure corresponding to the second configuration, as shown in Fig. 1(b). A similar calculation is done for this configuration in the presence of grating for various structural parameters such as segment number, segmented metal film thickness, and thickness of the continuum part of the metal layer. A typical SPR mode profile for the grated dual-core PCF-SPR sensor is presented in Fig. 7. Simultaneously localized SPR and propagated SPR in the neighborhood of the segment part are clearly observed.

The wavelength sensitivity, amplitude sensitivity, and figure of merit for the grated structure are computed and tabulated for different thicknesses of TiO_2 and also in the absence of the TiO_2 layer. Evidently, as shown in Table 3, in all cases of the presence of the extra TiO_2 layer, the proposed sensor shows better results in comparison with the bare one, the absence of the TiO_2 layer. Thus, TiO_2 has the definite effect on improving sensor detection sensitivity. It is seen that the maximum values of S_W, S_A, and FOM belong to grating configuration associated with 5 nm of TiO_2 thickness. Therefore, we continue our simulation with 5 nm thickness of TiO_2

The sensing parameters for different analyte refractive indexes of the grated structure with $t_{TiO_2} = 5\ nm$, $t_{Au} = 40\ nm$, and segment number of 28 are shown in Table 4. It can be concluded from this table that S_W, S_A, and FOM reach their maximum value when RI varies between 1.43 and 1.44.

Figure 8 shows the effect of N, segment number, on the wavelength sensitivity with and without the TiO_2 layer. Also in Table 5, the effects of this parameter on the other sensing factors are shown.

Fig. 6 Loss curves for thickness variation of TiO_2 for $n_a = 1.43$, $t_{Au} = 40\ nm$

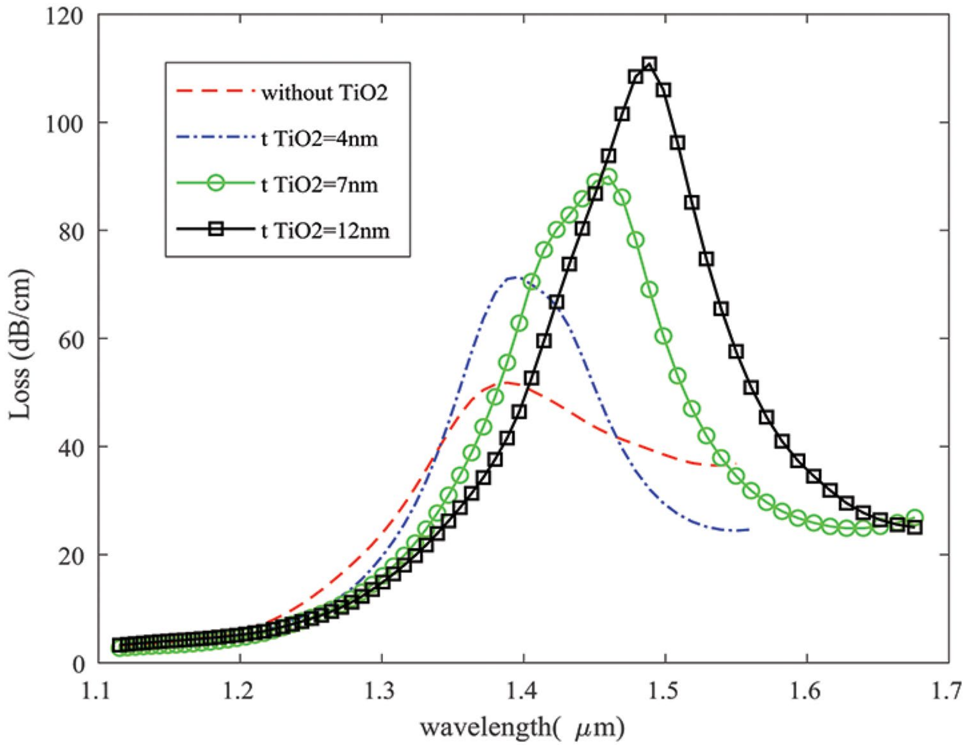

This figure depicted that the existence of the TiO_2 layer has a considerable role on S_w behavior. In fact, in the absence of TiO_2, when N increases, sensitivity varies in a zigzag form where it has a smooth behavior with a single peak value in the presence of TiO_2. The peak value in both cases occurs in $N = 28$. It is worth mentioning that the same calculation for N values smaller than 20 is done which gives sensitivities lower than the obtained peak value. Consequently, the

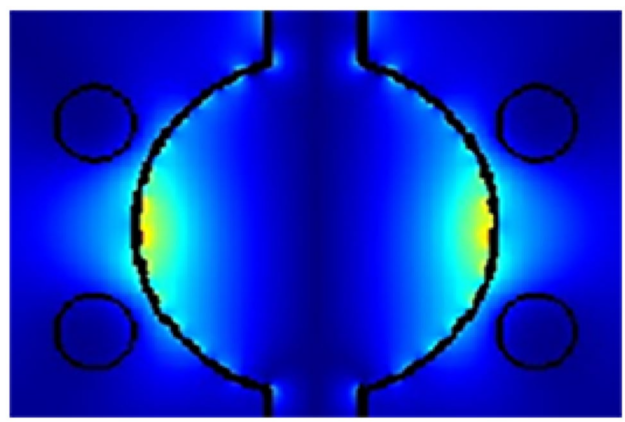

Fig. 7 Electric field distribution of the SPR mode for grated structure for $n_a = 1.43$

Table 1 Effect of gold thickness on S_w and S_A

Au thickness (nm)	Wavelength sensitivity $\left(S_W, \frac{nm}{RIU}\right)$	Amplitude sensitivity $\left(S_A, \frac{1}{RIU}\right)$
30	8728	292.3
40	15,167	411.1
50	14,768	263.2

Table 2 Performance analysis of the proposed sensor by varying the dielectric RI

Dielectric RI	$S_W\left(\frac{nm}{RIU}\right)$	$S_A\left(RIU^{-1}\right)$	FOM $\left(RIU^{-1}\right)$	Resolution (RIU)
1.42–1.43	15,167	411.1	207.19	6.6×10^{-6}
1.43–1.44	6894	314.5	62.55	1.4×10^{-5}
1.44–1.45	3158	59.95	35.40	3.1×10^{-5}
1.45–1.46	2179	19.8	22.91	4.6×10^{-5}

Table 3 Performance analysis of the proposed sensor for grating configuration by varying TiO_2 thicknesses

t_{TiO_2}	Maximum $S_W,\left(\frac{nm}{RIU}\right)$	Maximum $S_A,\left(\frac{1}{RIU}\right)$	$FOM,\left(\frac{1}{RIU}\right)$
0 nm	12,397	302.9	84.91
3 nm	12,068	408.4	150.85
5 nm	13,295	511.4	166.18
6 nm	9116	320.8	99.08
7 nm	12,638	260.8	133.03
10 nm	11,931	326.9	80.07

Table 4 Performance analysis of the proposed sensor for grating configuration by varying the dielectric RI

Dielectric RI	λ_{peak} (μm)	$S_W\left(\frac{nm}{RIU}\right)$	$S_A\left(RIU^{-1}\right)$	$FOM\ \left(RIU^{-1}\right)$
1.42	1.4046	5790	234.9	75.19
1.43	1.4625	13,295	511.4	166.18
1.44	1.5954	6282	124.5	73.90
1.45	1.6582	2655	16.27	39.04
1.46	1.6848	-	-	-

sensitivity can be effectively tuned by the segment number. We consider $N = 28$ as an optimized segment number.

From Table 5, it is observed that when N varies from 20 to 38, the maximum obtained wavelength, amplitude sensitivity, FOM, and average sensitivity are 13,295 $\frac{nm}{RIU}$, 511.4 RIU^{-1}, 166.18 RIU^{-1}, and 8455.6 $\frac{nm}{RIU}$ in the presence of the TiO_2 layer. The corresponding values decrease to 12,397 $\frac{nm}{RIU}$, 302.9 RIU^{-1}, 130.5 RIU^{-1}, and 8193 $\frac{nm}{RIU}$ in the absence of TiO_2. It is worth noting that these maximum values allocate to $N = 28$.

Considering the optimized values of $t_{Au} = 40\ nm$, $t_{TiO_2} = 5\ nm$, and $N = 28$, the effect of d_1 and d_2 on the sensor performance is considered simultaneously, with the condition of $d_1 + d_2 = 40\ nm$, $\left(d_1 + d_2 = t_{Au}\right)$. Results are shown in Fig. 9 which shows the loss spectra for different arrangements of d_1 and d_2. For arrangements of $d_1 = 30\ nm$ and $d_2 = 10\ nm$ when n_a changes from 1.42 to 1.45, the wavelength sensitivities are 7432, 10,467, 5805, and 3205 $\frac{nm}{RIU}$, while the corresponding values are 6379, 12,397, and 5805 $\frac{nm}{RIU}$ for the arrangement of $d_1 = 25\ nm$ and $d_2 = 15\ nm$.

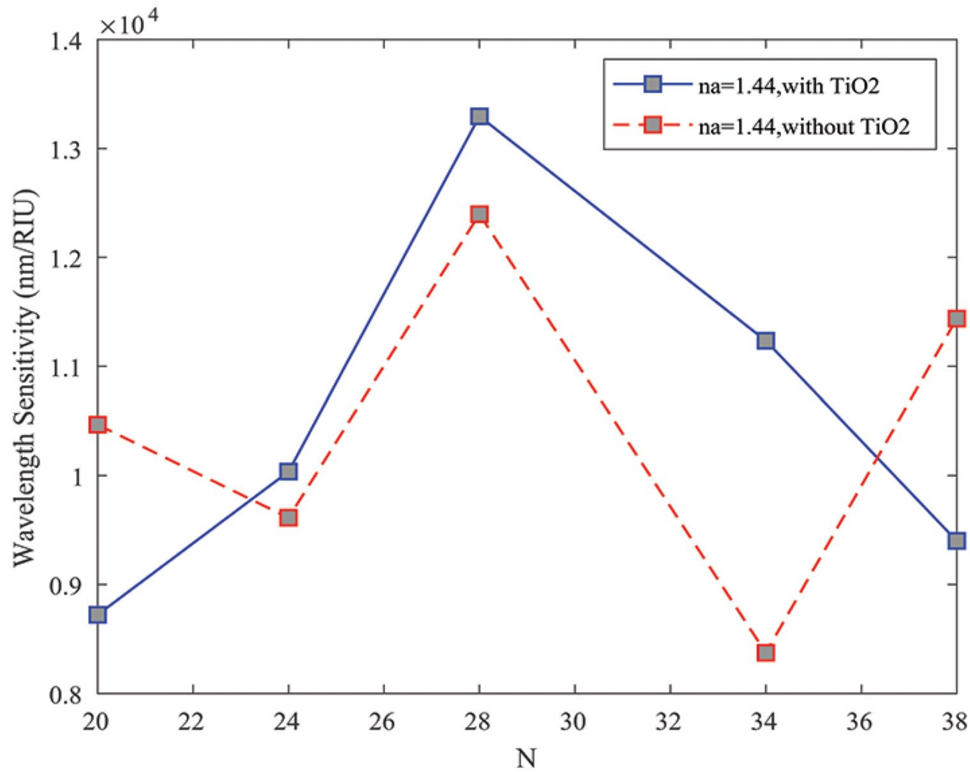

Fig. 8 Wavelength sensitivity of the core mode for different N for $n_a = 1.43$

Table 5 Effect of Au grated with 5 nm thickness of TiO_2 on S_w, S_A, FOM, and average sensitivity for different N

Segment number N	Maximum $S_w\left(\frac{nm}{RIU}\right)$		Maximum $S_A\left(RIU^{-1}\right)$		Maximum $FOM\left(RIU^{-1}\right)$		Average sensitivity	
	Without TiO_2	With TiO_2	Without TiO_2	With TiO_2	Without TiO_2	With TiO_2	Without TiO_2	With TiO_2
20	10,467	8722	285.4	301.3	73.71	96.91	5026	4899.3
24	9613	10,036	273.4	409.8	99.10	145.44	6101.6	6525.6
28	12,397	13,295	302.9	511.4	130.5	166.18	8193	8455.6
34	8373	11,235	283.4	472.5	64.90	160.5	5501.3	7521.6
38	11,438	9400	225.1	400	105.9	110.58	7503.3	6862.6

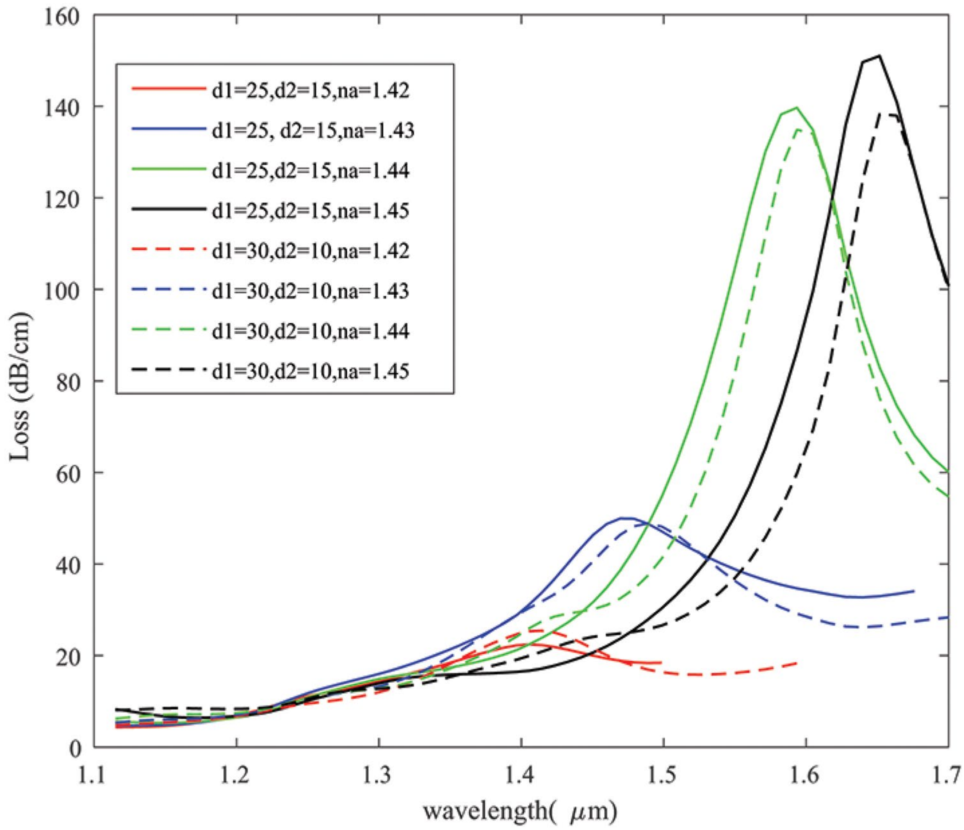

Fig. 9 Loss spectra as a function of different arrangements of d_1 and d_2

As a result, when $d_1 = 25\ nm$ and $d_2 = 15\ nm$, the maximum wavelength sensitivity is higher than that when the sensor is set with $d_1 = 30\ nm$ and $d_2 = 10\ nm$.

Conclusion

In summary, two different configurations of highly sensitive opening-up dual-core photonic crystal fiber sensors based on surface plasmon resonance have been introduced and numerical analyses have been performed by using the FDTD method. The opening-up structure not only simplifies analyte infiltration and gold coating but also offers the capacity for real-time sensing. The results reveal that the odd mode for *y*-polarization coupled with odd SPR mode more strongly due to its largest confinement loss in two structures. Additionally, a comparison was made in each configuration in the presence of TiO_2 and in the absence of TiO_2 in terms of the sensitivity and FOM. As regards applying the TiO_2 layer improving the sensitivity by about 16% for the first configuration and about 7% for the second configuration, it was observed that the dual-core SPR-PCF sensor with a TiO_2 thin layer without grating structure shows the highest sensing performance. Surprisingly, this sensor has the capability to detect higher or lower RI than the RI of the background material. Owning to the highly sensitive response, the proposed sensor can be considered ideal for refractive index detection.

Author Contribution Soghra Ghahramani: conceptualization, methodology, formal analysis and investigation, writing — original draft preparation. Jamal Barvestani: supervision, project administration, writing — review and editing. Bahar Meshginqalam: writing — review and editing.

Data Availability The datasets generated during the analysis of current study are available from the corresponding author on reasonable request.

Declarations

Ethics Approval This study does not involve human participants, as well as their data or biological material.

Consent to Participate Informed consent was obtained from all individual participants included in the study.

Consent for Publication The authors give consent for the publication of identifiable details within the text to be published in the *Plasmonics* journal.

Conflict of Interest The authors declare no competing interests.

References

1. Zhao Y et al (2019) Current status of optical fiber biosensor based on surface plasmon resonance. Biosens Bioelectron 142:111505
2. Wang J et al (2020) Surface plasmon resonance sensor based on coupling effects of dual photonic crystal fibers for low refractive indexes detection. Results in Phys 18:103240
3. Isti MIA et al (2020) Asymmetrical D-channel photonic crystal fiber-based plasmonic sensor using the wavelength interrogation and lower birefringence peak method. Results in Phys 19:103372
4. Liu C et al (2020) Near-infrared surface plasmon resonance sensor based on photonic crystal fiber with big open rings. Optik 207:164466
5. Hossain MB et al (2020) Numerical development of high performance quasi D-shape PCF-SPR biosensor: an external sensing approach employing gold. Results in Phys 18:103281
6. Paul AK et al (2020) An air-core photonic crystal fiber based plasmonic sensor for high refractive index sensing. Opt Commun 464:125556
7. Chen N et al (2019) Highly sensitive plasmonic sensor based on a dual-side polished photonic crystal fiber for component content sensing applications. Nanomaterials 9(11)
8. Rifat AA et al (2018) Highly sensitive selectively coated photonic crystal fiber-based plasmonic sensor. Opt Lett 43(4):891–894
9. Hasan MR et al (2018) Spiral photonic crystal fiber-based dual-polarized surface plasmon resonance biosensor. IEEE Sens J 18(1):133–140
10. Paul AK, Sarkar AK, Khaleque A (2019) Dual-core photonic crystal fiber plasmonic refractive index sensor: a numerical analysis. Photonic Sensors 9(2):151–161
11. Han H et al (2020) A large detection-range plasmonic sensor based on an H-shaped photonic crystal fiber. Sensors 20(4)
12. Haque E et al (2019) Highly sensitive dual-core PCF based plasmonic refractive index sensor for low refractive index detection. IEEE Photonics J 11(5):1–9
13. Haque E et al (2018) Surface plasmon resonance sensor based on modified *D*-shaped photonic crystal fiber for wider range of refractive index detection. IEEE Sens J 18(20):8287–8293
14. Luan N et al (2019) Opening up dual-core microstructured optical fiber-based plasmonic sensor with large detection range and linear sensitivity. Opt Mater Express 9(2):819–825
15. Luan N, Yao J (2016) Surface plasmon resonance sensor based on exposed-core microstructured optical fiber placed with a silver wire. IEEE Photonics J 8(1):1–8
16. Singh S, Prajapati YK (2020) TiO2/gold-graphene hybrid solid core SPR based PCF RI sensor for sensitivity enhancement. Optik 224:165525
17. van Brakel A et al (2007) Micro-channels machined in microstructured optical fibers by femtosecond laser. Opt Express 15(14):8731–8736
18. Wang F et al (2011) Selective filling of photonic crystal fibers using focused ion beam milled microchannels. Opt Express 19(18):17585–17590
19. Erdmanis M et al (2011) Comprehensive numerical analysis of a surface-plasmon-resonance sensor based on an H-shaped optical fiber. Opt Express 19(15):13980–13988
20. Cox FM et al (2007) Opening up optical fibres. Opt Express 15(19):11843–11848
21. Randolph SJ, Fowlkes JD, Rack PD (2006) Focused, nanoscale electron-beam-induced deposition and etching. Crit Rev Solid State Mater Sci 31(3):55–89
22. Boehm J et al (2011) Chemical deposition of silver for the fabrication of surface plasmon microstructured optical fibre sensors. Plasmonics 6(1):133–136
23. Vieweg M et al (2010) Ultrafast nonlinear optofluidics in selectively liquid-filled photonic crystal fibers. Opt Express 18(24):25232–25240
24. Chen W, Ahmed H (1993) Fabrication of 5–7 nm wide etched lines in silicon using 100 keV electron-beam lithography and polymethylmethacrylate resist. Appl Phys Lett 62(13):1499–1501
25. Otupiri R, Akowuah EK, Haxha S (2015) Multi-channel SPR biosensor based on PCF for multi-analyte sensing applications. Opt Express 23(12):15716–15727
26. DeVore JR (1951) Refractive indices of rutile and sphalerite. J Opt Soc Am 41(6):416–419
27. Hasan MR et al (2017) A highly sensitive gold-coated photonic crystal fiber biosensor based on surface plasmon resonance. Photonics 4(1)
28. Li T et al (2020) A refractive index sensor based on H-shaped photonic crystal fibers coated with Ag-graphene layers. Sensors 20(3)
29. Islam MS et al (2019) A Hi-Bi ultra-sensitive surface plasmon resonance fiber sensor. IEEE Access 7:79085–79094
30. Fang H et al (2020) Research on photonic crystal fiber based on a surface plasmon resonance sensor with segmented silver-titanium dioxide film. J Opt Soc Am B 37(3):736–744